Research Square

Preprints are preliminary reports that have not undergone peer review.
They should not be considered conclusive, used to inform clinical practice,
or referenced by the media as validated information.

Investigating the role of ferroptosis in the pathogenesis of murine models of metabolic dysfunction-associated steatohepatitis (MASH)

MINORU TANAKA

tanaka.m@jihs.go.jp

Japan Institute for Health Security

Marie Kijima

Japan Institute for Health Security

Kazuko Kanegae

Japan Institute for Health Security

Shinya Tsurusaki

The Westmead Institute for Medical Research

Cindy Kok

Children's Medical Research Instituite, Westmead

Masato Tanaka

Tokyo University of Pharmacy and Life Sciences https://orcid.org/0000-0001-9243-5906

Hiroyasu Nakano

Toho University https://orcid.org/0000-0003-4843-1427

Article

Keywords:

Posted Date: June 9th, 2026

DOI: https://doi.org/10.21203/rs.3.rs-9598743/v1

License: This work is licensed under a Creative Commons Attribution 4.0 International License.
Read Full License

Additional Declarations: (Not answered)

Abstract

Non-alcoholic steatohepatitis (NASH) is a chronic liver disease that develops from simple fatty liver and progresses to hepatitis, liver fibrosis, cirrhosis, and eventually liver cancer, in the absence of significant alcohol consumption. Recently, the term NASH has been replaced with metabolic dysfunction-associated steatohepatitis (MASH) on the basis of new diagnostic criteria. Cell death may lead to damage associated molecular patterns (DAMPs)-mediated inflammatory response and is therefore considered a key therapeutic target in chronic liver diseases. However, the impact of cell death on the long-term pathogenesis of MASH remains uncertain. We have reported that ferroptosis precedes apoptosis in lipid-accumulating hepatocytes, followed by hepatitis in a murine model of NASH. Because lipid peroxidation is an essential step in ferroptosis, glutathione peroxidase 4 (GPX4), which reduces phospholipid hydroperoxides, plays a crucial role in ferroptosis inhibition. However, the role of GPX4 in MASH remains unclear. Here, we investigated the role of ferroptosis in the pathogenesis of MASH by promoting or inhibiting ferroptosis in murine models of MASH. To promote ferroptosis, we generated liver-specific *Gpx4* knockout (*Gpx4* LKO) mice and fed them two distinct MASH diets. Although lipid peroxidation tended to increase in *Gpx4* LKO mouse liver compared with control mouse liver, no significant difference in liver fibrosis was noted between the two mouse groups, suggesting that enhancing ferroptosis had a limited influence on the pathology of MASH. In contrast, inhibiting ferroptosis by vitamin E administration reduced lipid peroxidation, ameliorating liver fibrosis. These results suggest that inhibiting ferroptosis is a promising therapeutic target in the long-term pathogenesis of MASH, whereas enhancing ferroptosis has a limited impact on liver fibrosis.

Introduction

Metabolic dysfunction-associated steatotic liver disease (MASLD), previously known as non-alcoholic fatty liver disease (NAFLD), comprises several pathological processes that begins with excessive triglyceride accumulation and gradually progresses toward metabolic dysfunction-associated steatohepatitis (MASH), liver fibrosis, cirrhosis, and liver cancer [ref. 1–4]. The number of patients is expected to increase further [ref. 5]. However, the details of MASH pathogenesis remain unclear, and effective treatments are lacking. Therefore, developing an effective treatment for MASH is an urgent priority. Various factors lead to liver disease, including alcohol, drugs, and immune and metabolic abnormalities. In all cases, cell death that triggers an immune cell-mediated inflammatory response is the primary pathophysiology of hepatitis. Therefore, cell death is considered a key event in liver disease progression.

Cell death is conventionally classified into apoptosis and necrosis [ref. 6]. Whereas apoptosis is programmed cell death mediated by intracellular signaling cascades, necrosis has been considered as an accidental type of cell death resulting from physical damage. The term “regulated cell death (RCD)” has been proposed to denote cell death regulated by intracellular molecules. RCD comprises apoptosis and necrotic cell death, such as necroptosis, pyroptosis, and ferroptosis. The role of RCD in various diseases has captured the attention of researchers [ref. 7]. Ferroptosis is a form of RCD caused by the

accumulation of iron-dependent lipid peroxides [ref. 8]. Iron contributes to lipid peroxidation via the Fenton reaction, and a series of molecules, including Gpx4 (glutathione peroxidase 4), have been identified as regulatory mechanisms [ref. 9]. The principal mechanism underlying ferroptosis involves the oxidation of polyunsaturated fatty acids (PUFAs), which results in lipid peroxidation that damages lipids in the cell membrane. Lipid hydroperoxides (LOOHs) are the primary products of the Fe^{2+}-dependent Fenton reaction. LOOHs can be degraded into secondary aldehydes, such as malondialdehyde (MDA), propanal, hexanal, and 4-hydroxynonenal (4-HNE) [ref. 10, 11], and these aldehydes function as lipid peroxidation markers, acting as the hallmark features of ferroptosis.

In contrast, Gpx4, a pivotal enzyme in the antioxidant system, uses reduced glutathione (GSH) to reduce lipid peroxides produced by reactive oxygen species (ROS) [ref. 12]. Therefore, reduced Gpx4 activity and intracellular GSH depletion promote ferroptosis by accumulating lipid peroxides. We have previously reported that ferroptosis occurs in lipid-accumulating hepatocytes, triggering inflammation and NASH development [ref. 13]. However, the role of ferroptosis in the long-term pathogenesis of MASH remains unknown. In this study, we investigated the impact of ferroptosis in murine models of MASH by promoting or inhibiting ferroptosis using liver-specific *Gpx4* knockout (*Gpx4* LKO) mice or administering a chemical inhibitor.

Results

Generation of murine model with liver-specific Gpx4 deletion

It is well established that Gpx4 plays a role in reducing lipid peroxide accumulation, which causes ferroptosis. To investigate the impact of ferroptosis on the pathogenesis of MASH, we generated a murine model in which *Gpx4* was deleted from hepatocytes. Although it has been reported that *Gpx4* LKO mice were generated by crossing *Albumin-Cre* transgenic (tg) mice with *Gpx4*-floxed ($Gpx4^{Flox/Flox}$) mice, the *Gpx4* LKO mice were embryonic lethal [ref. 14]. To avoid lethality in the *Gpx4* LKO mice during the developmental stage, we attempted to deliver an improved Cre (*iCre*) gene into adult $Gpx4^{Flox/Flox}$ mice after birth via an Adeno-associated virus 8 (AAV8) vector. First, we injected the AAV8-iCre vector into CAG-lsl-tdTomato reporter mice. Two weeks later, we detected strong tdTomato fluorescence in the AAV8-iCre-injected mouse liver compared with the AAV8-GFP-injected control (ctrl) by fluorescence microscopy (Fig. 1a). Similarly, the AAV8-GFP-injected mouse liver showed strong GFP fluorescence (Fig. 1b). Because these results suggested that gene delivery by the AAV vector generates *Gpx4* LKO mice after birth, we injected AAV8-iCre or AAV8-GFP vector into 8-week-old $Gpx4^{Flox/Flox}$ mice for further analyses (Fig. 1c). To investigate the impact of ferroptosis on the pathology of MASH, *Gpx4* LKO mice were fed MASH diet, Gubra Amylin (GAN) for 40 weeks. We confirmed that *Gpx4* expression was significantly lower in *Gpx4* LKO mouse liver than in ctrl by quantitative RT-PCR analysis (Fig. 1d). Consistently, immunostaining and western blotting of liver samples with anti-Gpx4 antibody revealed that Gpx4 expression apparently decreased in *Gpx4* LKO mouse liver compared with ctrl (Figs. 1e and f, Original WD1), indicating that the loss of Gpx4 persisted in the liver of *Gpx4* LKO mice fed GAN diet for 40 weeks. Ferroptosis suppressor protein 1 (*Fsp1*) is known to confer protection against ferroptosis

elicited by GPX4 deletion [ref. 15]. However, we found no significant difference in *Fsp1* expression between ctrl and *Gpx4* LKO mice (Fig. 1g). Consistent with the decrease in *Gpx4* expression, 2-thiobarbituric acid reactive substances (TBARS) assay and immunostaining of 4-HNE revealed an increase in lipid peroxide levels in *Gpx4* LKO mouse liver (Figs. 1h and i), suggesting that ferroptosis seemed to be enhanced in *Gpx4* LKO mouse liver owing to the decrease in Gpx4 activity.

Evaluation of MASH pathology in Gpx4 LKO mouse

We next compared MASH pathology between ctrl and *Gpx4* LKO mice. H&E staining revealed no differences in lipid accumulation between the two mouse groups (Fig. 2a). We also measured serum liver injury markers, aspartate aminotransferase (AST) and alanine aminotransferase (ALT), at several time points after feeding GAN diet. Although serum ALT levels gradually increased over time after feeding GAN diet irrespective of genotype, no significant difference was observed between ctrl and *Gpx4* LKO mice (Fig. 2b and Table 1). Hepatic macrophages are known to form crown-like structures in the pathogenesis of MASH [ref. 16]. Immunostaining with anti-CD11b antibody showed comparable infiltration of inflammatory cells between ctrl and *Gpx4* LKO mice (Fig. 2c). Additionally, the expression profiles of inflammatory cytokines *Il1b*, *Il6*, and *Tnf w*ere not significantly different between ctrl and *Gpx4* LKO mice (Fig. 2d). To assess the status of liver fibrosis, we performed Picro-Sirius Red staining and immunostaining with anti-Collagen I antibody, but found no significant difference in liver fibrosis area between ctrl and *Gpx4* LKO mice (Fig. 2e). Similarly, there was no significant difference in the expression profiles of fibrosis-related genes, *Collagen 1a1* (*Col1a1*), Transforming growth factor (*Tgfb*), and Connective tissue growth factor (*Ctgf*) (Fig. 2f). Together, these results suggest that the enhancement of ferroptosis has a minimal influence on MASH progression in the GAN diet murine model.

Evaluation of MASH pathology in CDAHFD-fed Gpx4 LKO mouse

Several murine models of MASH are known, in addition to the GAN diet murine model. To confirm the phenotype of *Gpx4* LKO mice in the pathogenesis of MASH, we tested another MASH diet, a choline-deficient, amino acid-defined high-fat diet (CDAHFD) (Supplemental Figures S1a) [ref. 17]. As with the case of GAN diet, *Gpx4* LKO mice fed CDAHFD for 24 weeks showed that *Gpx4* gene and protein expression levels were significantly downregulated (Supplemental Figures S1b, d, and e, Original WB2). There was also no significant difference in the expression profiles of *Fsp1* (Supplemental Figures S1c). TBARS assay and immunostaining indicated elevated lipid peroxidation in *Gpx4* LKO mouse liver, as evidenced by an increase in 4-HNE-positive area, suggesting enhanced ferroptosis (Figs. 3a and b). On the other hand, the levels of inflammatory cell infiltration and liver fibrosis were comparable between ctrl and *Gpx4* LKO mice fed CDAHFD (Figs. 3c–e). Taken together, these results suggest that the loss of hepatic Gpx4 has a limited impact on MASH progression even in known dietary models.

Ferroptosis inhibition by vitamin E administration ameliorates liver fibrosis

Although the enhancement of ferroptosis by hepatic Gpx4 depletion marginally affected liver fibrosis in MASH, the impact of ferroptosis inhibition remains unclear. Vitamin E has been reported to inhibit ferroptosis [ref. 12]. Therefore, we tested whether vitamin E inhibits ferroptosis in the CDAHFD model. To this end, α-tocopherol, a lipid antioxidant, was added to CDAHFD at 1,000 IU/kg. Wild-type mice were fed CDAHFD alone (ctrl) or CDAHFD containing vitamin E (CDAHFD + E) for 8 weeks, respectively (Fig. 4a). Lipid accumulation in the liver was comparable between the two mouse groups (Fig. 4b, top figure). However, autofluorescence, which reflects liver damage, was markedly downregulated in the CDAHFD + E mouse group compared with ctrl (Fig. 4b, bottom figure). Consistent with the decrease in autofluorescence, TBARS assay (Fig. 4c) and immunostaining for 4-HNE (Fig. 4d) revealed reduced lipid peroxidation in the CDAHFD + E mouse group. Concomitantly, the expression of inflammatory cytokines *Il1b, Il6, and Tnf* was downregulated in the CDAHFD + E mouse group compared with ctrl (Fig. 4e). Intriguingly, immunostaining with anti-Cleaved caspase-3 (CC3) antibody revealed that the number of apoptotic cells was significantly lower in the CDAHFD + E mouse group than ctrl (Fig. 4f). Furthermore, immunostaining with anti-CD11b antibody and quantitative RT-PCR of fibrosis-related genes indicated that liver fibrosis was ameliorated in the CDAHFD + E mouse group compared with ctrl (Figs. 4g–i). These results suggest that inhibiting ferroptosis alleviates MASH pathogenesis, including liver fibrosis, whereas enhancing ferroptosis via hepatic Gpx4 depletion has a marginal effect.

Apoptosis contributes to the exacerbation of liver fibrosis

Whereas liver fibrosis was not exacerbated by enhancing ferroptosis, it was ameliorated by inhibiting ferroptosis, reducing the number of apoptotic cells. Given these findings, apoptosis may be more relevant to the progression of liver fibrosis than ferroptosis. Because cellular FLICE-inhibitory protein is a potent anti-apoptotic factor that directly inhibits caspase-8 activation, cells deficient in its encoding gene, *Cflar*, exhibit increased susceptibility to apoptosis [ref. 18]. In fact, we previously reported that liver-specific *Cflar* KO (*Cflar* LKO) mice fed a choline-deficient, ethionine-supplemented (CDE) NASH diet exhibited exacerbation of liver fibrosis accompanied by increased numbers of apoptotic cells [ref. 19]. The pathological features of apoptosis, inflammation, and liver fibrosis were exacerbated in *Cflar* LKO mice after feeding the CDE diet for 3 weeks (Supplemental Figure S2a-f).

To investigate the contribution of apoptosis to liver fibrosis in another murine model of MASH, we fed *Cflar* LKO mice CDAHFD and analyzed the liver after 8 weeks (Fig. 5a). As expected, immunostaining for CC3 demonstrated a significant increase in the number of apoptotic cells in *Cflar* LKO mouse liver compared with *Cflar* floxed ctrl mouse liver (Fig. 5b). Accordingly, the number of infiltrated CD11b-positive inflammatory cells significantly increased in *Cflar* LKO mouse liver (Fig. 5c). Although gene expression of inflammatory cytokines was comparable between genotypes (Fig. 5d), fibrosis-related gene expression and Picro-Sirius Red staining revealed that liver fibrosis was exacerbated in *Cflar* LKO mice compared with ctrl mice (Figs. 5e and f)

Discussion

MASLD is the most common liver disease worldwide. It is characterized by the presence of steatosis in more than 5% of hepatocytes. A subset of MASLD patients progress to MASH, which is accompanied by hepatocyte ballooning and lobular inflammation caused by hepatocyte death. Because MASH can lead to advanced liver fibrosis, therapy for arresting disease progression is desired. Hepatocyte death can trigger inflammation via DAMPs release, rendering it a potential therapeutic target. In the past few decades, several types of RCD, including necroptosis, pyroptosis, and ferroptosis, have been reported in the context of disease pathogenesis [ref. 7]. In MASH, numerous studies have employed genetically modified mice and various murine models of NASH/MASH [ref. 20–25]. Those studies partially demonstrate the involvement of several types of cell death in the pathogenesis of MASH, including liver fibrosis. However, their importance is still under debate because of the diversity of experimental designs. Meanwhile, we previously reported that necrosis, including ferroptosis, precedes apoptosis at the onset of steatohepatitis [ref. 13]. In addition, inhibiting ferroptosis suppressed subsequent inflammation in a murine model of NASH. These findings motivated us to investigate the impact of ferroptosis on the long-term pathogenesis of MASH, including liver fibrosis. Hence, we hypothesized that enhancing hepatic ferroptosis would exacerbate liver fibrosis.

To test our hypothesis, we focused on Gpx4 function in the liver. Among the family of glutathione peroxidases, Gpx4 can reduce lipid hydroperoxides in biological membranes at the expense of reduced glutathione. Therefore, Gpx4 plays a crucial role in protecting biological membranes, and reduced Gpx4 activity leads to the accumulation of lipid peroxides, thereby triggering ferroptosis. In fact, it has been reported that *Gpx4* homozygous KO (*Gpx4*$^{-/-}$) mouse embryos die *in utero* by E7.5 [ref. 26, 27]. In addition, liver-specific *Gpx4* KO mice, generated by crossing *Gpx4*$^{Flox/Flox}$ mice with *Alb-Cre* tg mice, are also embryonically lethal [ref. 14]. These reports strongly suggest the critical role of Gpx4 in murine development. To avoid embryonic lethality and enhance ferroptosis in the liver, we generated adult *Gpx4* LKO mice by introducing iCre via an AAV8 vector after birth. This system worked well because *Gpx4* LKO mice could survive under the feeding of MASH diets. Unexpectedly, however, *Gpx4* LKO mice did not exhibit exacerbation of liver fibrosis compared with ctrl mice in two distinct murine MASH models, although ferroptosis was enhanced, as evidenced by the increased lipid peroxides in *Gpx4* LKO mouse liver. Because several types of cell death may occur in MASH, cell deaths other than ferroptosis may contribute more to liver fibrogenesis.

In contrast to the enhancement of ferroptosis, the inhibition of ferroptosis ameliorated the progression of liver fibrosis. It is widely accepted that vitamin E plays a role in inhibiting ferroptosis by counteracting oxidative damage to lipids and protecting biological membranes. Consistently, it has been reported that the administration of vitamin E to mother mice prolonged the lives of *Gpx4* KO pups when they were generated by crossing *Alb-Cre* tg mice with *Gpx4*-floxed mice [ref. 14]. It has also been reported that high concentrations of vitamin E in liver cells of hibernating Syrian hamsters prevented hepatic damage caused by low temperatures [ref. 28]. Presa et al. previously reported that vitamin E effectively ameliorated NASH pathology in *Pemt* KO mice [ref. 29]. In humans, vitamin E has been reported to improve serum ALT and AST levels and histology in adults with MASH, although it does not reduce

fibrosis [ref. 30]. In our experiment using the murine model of MASH, the addition of vitamin E to CDAHFD alleviated lipid peroxide accumulation, inflammatory cell infiltration, and liver fibrosis. Intriguingly, vitamin E seemed to suppress ferroptosis as well as apoptosis. Because we previously reported that ferroptosis occurs at the onset of NASH, followed by apoptosis, suppressing ferroptosis with vitamin E may lead to a decrease in apoptotic hepatocytes [ref. 13]. In another study on *Cflar* LKO mice, apoptosis enhancement contributed to the exacerbation of liver fibrosis [ref. 19]. Given these results, apoptosis may be a promising therapeutic target for liver fibrosis. Consistent with this idea, Emricasan, a pan-caspase inhibitor, has been developed as a therapeutic agent for MASH [ref. 31]. However, although Emricasan did not improve liver histology in human patients, it ameliorated MASH pathology, including NAS activity score and liver fibrosis, in a murine model [ref. 32]. Because it is well established that inhibiting one type of cell death induces a shift to another type, e.g., from apoptosis to necroptosis, a comprehensive study of RCDs in the pathogenesis of MASH is required.

Considering the difference in the phenotype of liver fibrosis between murine models of MASH and human patients after treatment, dealing with a therapeutic drug for liver fibrosis remains a significant challenge. In this regard, not only RCD but also its surrounding microenvironment should be considered to understand the mechanisms of liver fibrosis. Although we examined inflammatory macrophages, it would also be worthwhile to investigate the roles of T cells, B cells, and dendritic cells in RCD. In this report, we provide a new model for investigating the role of ferroptosis in liver diseases. Further serial analyses of interactions between inflammatory cells and hepatic stellate cells will delineate the role of each RCD type in the pathogenesis of MASH.

Declarations

Acknowledgement

This work was supported by Japan Agency for Medical Research and Development (AMED) under Grant Number JP23gm1210002 (to M.T., M.T. and H.N.), JP 25bk0104189, 25fk0210176, and JIHS Intramural Research Fund (24A2003 and 26A1008) (to M.T.), Japan Society for the Promotion of Science (JSPS) KAKENHI Grant-in-Aid for Early-Career Scientists Number JP23K15058 (to M.K.) and Japan Liver Disease Support Foundation (to M.K.). We also thank the members of the Kanto and Okochi laboratory for discussion and advices.

Conflict of Interest

The authors declare that they have no conflict of interest.

Materials and methods

Animals and murine models of MASH

Male C57BL/6J mice were purchased from Clea Japan, Inc. (Tokyo, Japan). *Gpx4*$^{Flox/Flox}$ and *Alb-Cre* tg mice were purchased from the Jackson Laboratory. *Cflar*$^{Flox/Flox}$mice were provided by Y-W. He and described previously. All animals were maintained in a standard specific-pathogen-free room at our animal facility. All mouse studies were conducted in accordance with institutional procedures and approved by the Animal Care and Use Committee of the National Center for Global Health and Medicine. To generate murine models of MASH, we fed 8-week-old mice GAN diet (D09100310N, Research Diets, NJ, USA) or CDAA-based high-fat diet (CDAHFD, A06071302, Research Diets, NJ, USA). To inhibit ferroptosis, vitamin E (α-tocopherol) was added to CDAHFD at a concentration of 1000 IU/kg as "CDAHFD+E". Liver and blood samples were collected at designated time points for further analyses.

To deplete *Cflar* in mouse liver, *Cflar*$^{Flox/Flox}$ mice were crossed with *Alb-Cre* transgenic tg mice to generate *Cflar*$^{Flox/Flox}$*; Alb-Cre* mice [ref. 33]. We placed 12-week-old mice on a CDE diet (choline-depleted, ethionine-added chow; A06071302, Research Diets, NJ, USA) and collected liver and blood samples for further analysis.

Preparation of AAV8-iCre and AAV8-GFP vectors

AAV-293T cells were cultured in a 10 cm gelatin-coated dish (Corning, NY, USA) using Dulbecco's modified Eagle's medium (DMEM) culture medium (high glucose, D5796; Sigma-Aldrich, MO, USA) supplemented with 10% fetal bovine serum (FBS). After passaging AAV-293T cells at a concentration of 4 x 10^6 cells/well, the culture medium was exchanged for DMEM supplemented with 5% FBS. Transfection was performed as follows. First, a transfection reagent was prepared by mixing 3.3 μg of expression vector (pam.lsp-iCre, pam.lsp-GFP) (courtesy of Dr. Ian Alexander, Children's Medical Research Institute, Westmead, Australia), 3.3 μg of capsid vector (p5e18-vd2/8) (courtesy of Dr. James M Wilson, University of Pennsylvania, Philadelphia, PA), and 3.3 μg of helper vector (pXX6) (courtesy of Dr. Jude Samulski, University of North Carolina, Chapel Hill) in 33 μL of polyethylenimine "Max" diluted with 333 μL of Opti-MEM per 100 mm tissue culture dish. After 6 h of transfection, this treatment was repeated. The culture medium was replaced with DMEM containing 2% FBS once daily for 3 days. Subsequently, 0.5 M EDTA (pH 8.0) was added to a final concentration of 6.25 mM, and the detached cells were collected by centrifugation at 2000 x g for 10 min at 4 ˚C. The cell suspension was centrifuged at 2000 x g for 1 min at 4 ˚C, and the supernatant was completely removed. The AAV8 vector was purified from the cell precipitate in accordance with the instructions in the AAVpro Purification Kit (Takara, AAVpro Purification Kit Maxi (All Serotypes)). The titers of the AAV8 vector were determined by quantitative PCR (qPCR) using a LightCycler 480 System (Roche, Switzerland) with primers AAV 1361R (reverse: 5'–AGCTGACAGGTGGTGGCAAT–3') and AAV 1277F (forward: 5'–CCGTTGTCAGGCAACGTG–3').

Western blot

Proteins in liver tissues were extracted with RIPA lysis buffer, and concentrations were measured by the Bradford protein assay. Protein samples were electrophoresed on polyacrylamide gels and transferred

onto PVDF membranes. Membranes were blocked with 5% skim milk in PBS and incubated with anti-Gpx4 rabbit antibody (ab125066; Abcam, JPN, 1:500) and anti-GAPDH rabbit antibody (14C10; CST, MA, USA, 1:1000) at 4 °C overnight. After washing with TBST, membranes were incubated with secondary antibody at room temperature for 60 min and washed with TBST. The immunoblot was developed using Clarity™ Western ECL Substrate (Bio-Rad, CA, USA) and imaged in accordance with the manufacturer's protocol. Protein bands were semi-quantitatively analyzed using ImageJ.

Measurement of serum ALT and AST

Serum liver injury markers, ALT and AST, were measured using Transaminase C-II Test Wako (Wako, Japan) in accordance with the manufacturer's instructions. ALT and AST were measured at 555 nm using an EnVision plate reader (PerkinElmer, MA, USA) or an Infinite M Plex (TECAN, Switzerland).

Hematoxylin-eosin (H&E) and Picro-Sirius Red staining

Mouse livers were excised, fixed in 4% formalin, and embedded in paraffin. Liver paraffin sections (3 μm) were mounted on glass slides for H&E staining. To evaluate liver fibrosis, Picro-Sirius Red staining was performed, as described previously [ref. 13].

Immunohistochemistry (IHC) using DAB staining

Liver paraffin sections (3 μm) were mounted on glass slides for IHC. Immunohistochemical staining was performed by incubating liver samples with a primary antibody against Gpx4, 4-HNE, Cleaved caspase-3 (CC3), Collagen I, and CD11b. All images were acquired with an All-in-one BZX-710 (Keyence, Japan). Antibodies are listed in Table2.

Table 2: Used antibodies for IHC

antibody	concentration
Gpx4 (ab125066 rabbit mAb; Abcam, JPN)	1: 50
4-HNE (bs-6313R rabbit pAb; Bioss, MA, USA)	1: 200
CC3 (Asp175, 5A1E rabbit mAb; CST, MA, USA)	1: 150
Collagen I (ab21286 rabbit pAb; Abcam, JPN)	1: 300
CD11b (EPR1344, ab133357 rabbit mAb; Abcam, JPN)	1: 4000

TBARS assay

Lipid peroxidation levels in the liver were measured by an OxiSelect™ TBARS Assay Kit (Cell Biolabs, Inc., CA, USA). Approximately 25–50 mg of samples was extracted from liver tissues with PBS (-) buffer. TBARS assay was performed in accordance with the manufacturer's instructions. BHT was added before homogenization. Briefly, the homogenates were mixed with TBA reagents (pH 3.5) and incubated at 95

°C for 1 h. After incubation for 5 min on ice, the samples were centrifuged at 3000 rpm for 15 min at 4 °C. N-butanol was added before measurement, and absorbance was measured at 540 nm using the EnVision plate reader (PerkinElmer, MA, USA). TBARS concentration was normalized to the protein amount.

Quantitative analysis of fibrosis

Collagen fiber accumulation in the liver was evaluated using BZ-X710 and BZ-X Viewer (Keyence, Japan) after images of Picro-Sirius Red staining and immunohistochemistry with anti-Collagen I antibody were acquired. Mean ± s.d. from three random microscope images per mouse liver sample were quantified. Fibrotic regions were identified as red- or brown-colored areas using the Keyence BZ analyzer. The number of cells immunostained with anti-CD11b and anti-CC3 antibodies was quantified by using the Hybrid Cell Count function of the Keyence BZ analyzer.

Total RNA extraction and quantitative RT-PCR

Total RNA was extracted from liver tissues using TRIzol reagent (Invitrogen, MA, USA). cDNA was synthesized from RNA with PrimeScript RT Master Mix (Takara, Japan) for quantitative RT-PCR. Expression levels normalized to *Gapdh* were analyzed using the LightCycler 480 System (Roche, Switzerland). Primer sequences are listed in Table 3.

Table 3: Primer sequences for quantitative RT-PCR

Gene	Forward primer sequence (5'→3')	Reverse primer sequence (5'→3')
Gpx4	CTGCAACAGCTCCGAGTTC	GTTCCATTTGATGGCACTGG
Il1b	AGTTGACGGACCCCAAAAG	AGCTGGATGCTCTCATCAGG
Il6	GCTACCAAACTGGATATAATCAGGA	CCAGGTAGCTATGGTACTCCAGAA
Tnf	TCTTCTCATTCCTGCTTGTGG	GGTCTGGGCCATAGAACTGA
Col1a1	CATGTTCAGCTTTGTGGACCT	GCAGCTGACTTCAGGGATGT
Tgfb	TGGAGCAACATGTGGAACTC	CAGCAGCCGGTTACCAAG
Ctgf	GTGTGTGACCAGGCAGTGAT	AAGGGCAGAAAGTTGGTGTC
Fsp1	TGCAATGGGATCAAGATCAA	CACTTTCAGAGCACCATTGC
Gapdh	GCATCCACTGGTGCTGCC	TCATCATACTTGGCAGGTTTC

Statistical analyses

Statistical analyses were performed using GraphPad Prism (version 10.1.2). For comparison between two groups, a two-tailed unpaired Student's *t*-test was used. A *P* value of < 0.05 was considered

statistically significant. The exact number of biological samples is indicated in each figure legend. No outliers were excluded from the analyses.

References

1. Brunt EM, Janney CG, Di Bisceglie AM, Neuschwander-Tetri BA, Bacon BR. Nonalcoholic steatohepatitis: a proposal for grading and staging the histological lesions. Am J Gastroenterol. 1999;94(9):2467–74.
2. Angulo P. Nonalcoholic fatty liver disease. N Engl J Med. 2002;346(16):1221–31.
3. Rinella ME, Lazarus JV, Ratziu V, Francque SM, Sanyal AJ, Kanwal F, et al. A multisociety Delphi consensus statement on new fatty liver disease nomenclature. Hepatology. 2023;78(6):1966–86.
4. Liao Y, Chen Q, Liu L, Huang H, Sun J, Bai X, et al. Amino acid is a major carbon source for hepatic lipogenesis. Cell Metab. 2024;36(11):2437–48.e8.
5. Guo Z, Wu D, Mao R, Yao Z, Wu Q, Lv W. Global burden of MAFLD, MAFLD related cirrhosis and MASH related liver cancer from 1990 to 2021. Sci Rep. 2025;15(1):7083.
6. D'Arcy MS. Cell death: a review of the major forms of apoptosis, necrosis and autophagy. Cell Biol Int. 2019;43(6):582–92.
7. Tong X, Tang R, Xiao M, Xu J, Wang W, Zhang B, et al. Targeting cell death pathways for cancer therapy: recent developments in necroptosis, pyroptosis, ferroptosis, and cuproptosis research. J Hematol Oncol. 2022;15(1):174.
8. Dixon SJ, Lemberg KM, Lamprecht MR, Skouta R, Zaitsev EM, Gleason CE, et al. Ferroptosis: an iron-dependent form of nonapoptotic cell death. Cell. 2012;149(5):1060–72.
9. Yan HF, Zou T, Tuo QZ, Xu S, Li H, Belaidi AA, et al. Ferroptosis: mechanisms and links with diseases. Signal Transduct Target Ther. 2021;6(1):49.
10. Ayala A, Muñoz MF, Argüelles S. Lipid peroxidation: production, metabolism, and signaling mechanisms of malondialdehyde and 4-hydroxy-2-nonenal. Oxid Med Cell Longev. 2014;2014:360438.
11. Zhang X, Hou L, Guo Z, Wang G, Xu J, Zheng Z, et al. Lipid peroxidation in osteoarthritis: focusing on 4-hydroxynonenal, malondialdehyde, and ferroptosis. Cell Death Discov. 2023;9(1):320.
12. Stockwell BR, Friedmann Angeli JP, Bayir H, Bush AI, Conrad M, Dixon SJ, et al. Ferroptosis: A Regulated Cell Death Nexus Linking Metabolism, Redox Biology, and Disease. Cell. 2017;171(2):273–85.
13. Tsurusaki S, Tsuchiya Y, Koumura T, Nakasone M, Sakamoto T, Matsuoka M, et al. Hepatic ferroptosis plays an important role as the trigger for initiating inflammation in nonalcoholic steatohepatitis. Cell Death Dis. 2019;10(6):449.
14. Carlson BA, Tobe R, Yefremova E, Tsuji PA, Hoffmann VJ, Schweizer U, et al. Glutathione peroxidase 4 and vitamin E cooperatively prevent hepatocellular degeneration. Redox Biol. 2016;9:22–31.

15. Doll S, Freitas FP, Shah R, Aldrovandi M, da Silva MC, Ingold I, et al. FSP1 is a glutathione-independent ferroptosis suppressor. Nature. 2019;575(7784):693–698.
16. Itoh M, Kato H, Suganami T, Konuma K, Marumoto Y, Terai S, et al. Hepatic crown-like structure: a unique histological feature in non-alcoholic steatohepatitis in mice and humans. PLoS One. 2013;8(12):e82163.
17. Yasuda D, Torii H, Shimizu R, Hiraoka Y, Kume N. Reduced Serum Cholesterol and Triglyceride Levels in a Choline-Deficient L-Amino Acid-Defined High-Fat Diet (CDAHFD)-Induced Mouse Model of Non-alcoholic Steatohepatitis (NASH). Biol Pharm Bull. 2020;43(4):616–8.
18. Safa AR, Day TW, Wu CH. Cellular FLICE-like inhibitory protein (C-FLIP): a novel target for cancer therapy. Curr Cancer Drug Targets. 2008;8(1):37–46.
19. Tsuchiya Y, Seki T, Kobayashi K, Komazawa-Sakon S, Shichino S, Nishina T, et al. Fibroblast growth factor 18 stimulates the proliferation of hepatic stellate cells, thereby inducing liver fibrosis. Nat Commun. 2023;14(1):6304.
20. Thapaliya S, Wree A, Povero D, Inzaugarat ME, Berk M, Dixon L, et al. Caspase 3 inactivation protects against hepatic cell death and ameliorates fibrogenesis in a diet-induced NASH model. Dig Dis Sci. 2014;59(6):1197–206.
21. Gautheron J, Vucur M, Reisinger F, Cardenas DV, Roderburg C, Koppe C, et al. A positive feedback loop between RIP3 and JNK controls non-alcoholic steatohepatitis. EMBO Mol Med. 2014;6(8):1062–74.
22. Roychowdhury S, McCullough RL, Sanz-Garcia C, Saikia P, Alkhouri N, Matloob A, et al. Receptor interacting protein 3 protects mice from high-fat diet-induced liver injury. Hepatology. 2016;64(5):1518–33.
23. Saeed WK, Jun DW, Jang K, Ahn SB, Oh JH, Chae YJ, et al. Mismatched effects of receptor interacting protein kinase-3 on hepatic steatosis and inflammation in non-alcoholic fatty liver disease. World J Gastroenterol. 2018;24(48):5477–90.
24. Xu B, Jiang M, Chu Y, Wang W, Chen D, Li X, et al. Gasdermin D plays a key role as a pyroptosis executor of non-alcoholic steatohepatitis in humans and mice. J Hepatol. 2018;68(4):773–82.
25. Henao-Mejia J, Elinav E, Jin C, Hao L, Mehal WZ, Strowig T, et al. Inflammasome-mediated dysbiosis regulates progression of NAFLD and obesity. Nature. 2012;482(7384):179–85.
26. Yant LJ, Ran Q, Rao L, Van Remmen H, Shibatani T, Belter JG, et al. The selenoprotein GPX4 is essential for mouse development and protects from radiation and oxidative damage insults. Free Radic Biol Med. 2003;34(4):496–502.
27. Imai H, Hirao F, Sakamoto T, Sekine K, Mizukura Y, Saito M, et al. Early embryonic lethality caused by targeted disruption of the mouse PHGPx gene. Biochem Biophys Res Commun. 2003;305(2):278–86.
28. Anegawa D, Sugiura Y, Matsuoka Y, Sone M, Shichiri M, Otsuka R, et al. Hepatic resistance to cold ferroptosis in a mammalian hibernator Syrian hamster depends on effective storage of diet-derived α-tocopherol. Commun Biol. 2021;4(1):796.

29. Presa N, Clugston RD, Lingrell S, Kelly SE, Merrill AH, Jr., Jana S, et al. Vitamin E alleviates non-alcoholic fatty liver disease in phosphatidylethanolamine N-methyltransferase deficient mice. Biochim Biophys Acta Mol Basis Dis. 2019;1865(1):14–25.
30. Chee NM, Sinnanaidu RP, Chan WK. Vitamin E improves serum markers and histology in adults with metabolic dysfunction-associated steatotic liver disease: Systematic review and meta-analysis. J Gastroenterol Hepatol. 2024;39(12):2545–54.
31. Barreyro FJ, Holod S, Finocchietto PV, Camino AM, Aquino JB, Avagnina A, et al. The pan-caspase inhibitor Emricasan (IDN-6556) decreases liver injury and fibrosis in a murine model of non-alcoholic steatohepatitis. Liver Int. 2015;35(3):953–66.
32. Harrison SA, Goodman Z, Jabbar A, Vemulapalli R, Younes ZH, Freilich B, et al. A randomized, placebo-controlled trial of emricasan in patients with NASH and F1-F3 fibrosis. J Hepatol. 2020;72(5):816–27.
33. Piao X, Komazawa-Sakon S, Nishina T, Koike M, Piao JH, Ehlken H, et al. c-FLIP maintains tissue homeostasis by preventing apoptosis and programmed necrosis. Sci Signal. 2012;5(255):ra93.

Tables

Table 1 is available in the Supplementary Files section.

Figures

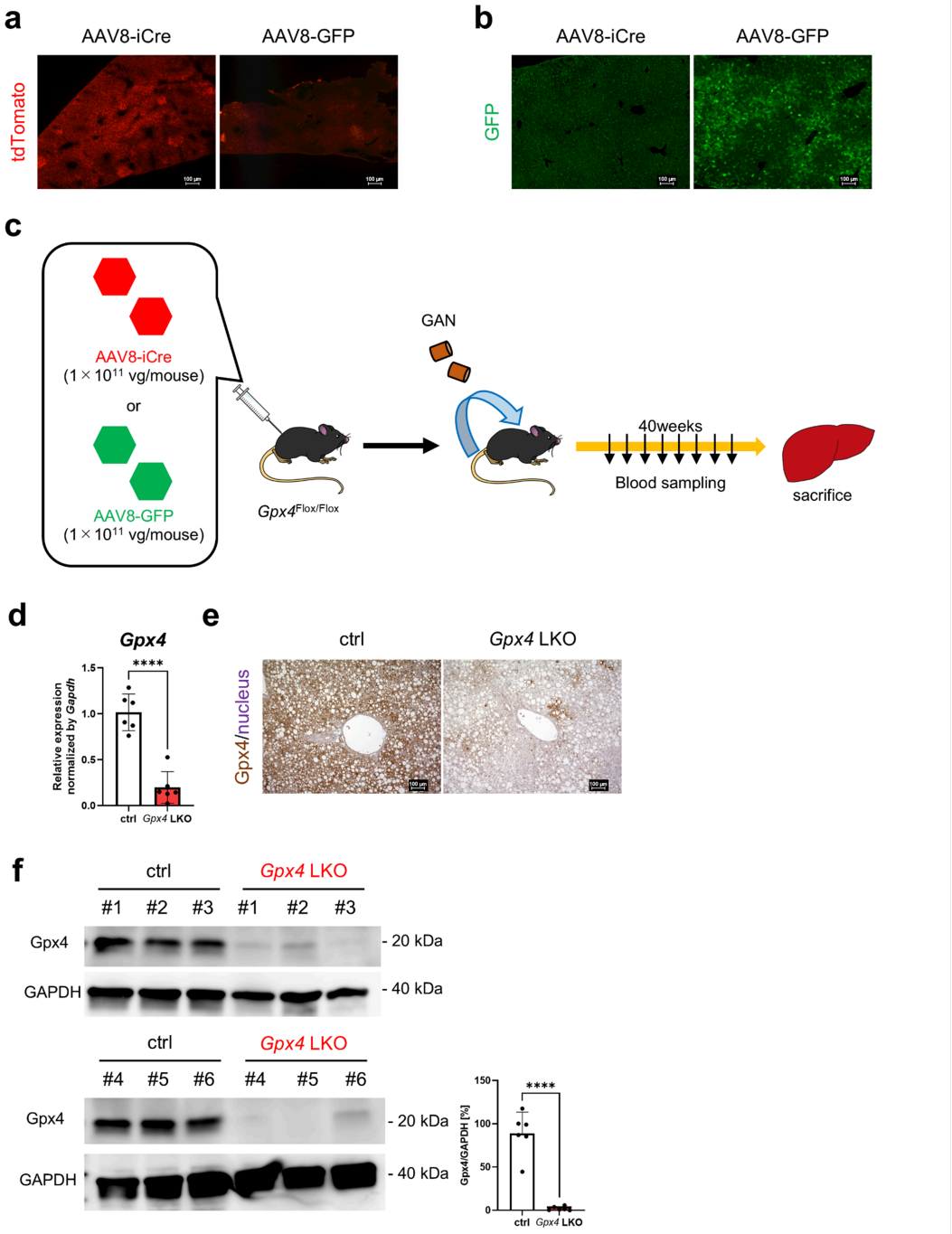


Figure 1

Figure 1

Generation of experimental murine model with liver-specific *Gpx4* deletion

(a) Fluorescence images of tdTomato in a frozen section of AAV8-iCre- or AAV8-GFP-transduced CAG-lsl-tdTomato reporter (Ai9) mice. tdTomato^{+} cells were observed in AAV8-iCre-transduced mouse liver. (b) Fluorescence images of GFP in a frozen section of AAV8-iCre- or AAV8-GFP- transduced C57BL/6

mouse. (c) Experimental design for the generation of control (ctrl) or *Gpx4* LKO mice by transducing $Gpx4^{Flox/Flox}$ mice with AAV8 vectors. (d) Quantitative RT-PCR analysis of *Gpx4* expression in the liver of ctrl or *Gpx4* LKO mice fed GAN diet for 40 weeks (n = 6). All data are normalized to *Gapdh*. (e) Immunohistochemical images of Gpx4 detected by DAB staining in the liver of ctrl or *Gpx4* LKO mice fed GAN diet for 40 weeks. (f) Western blot analysis of Gpx4 and GAPDH proteins in the liver extracts from ctrl or *Gpx4* LKO mice fed GAN diet for 40 weeks (n = 6). (g) Quantitative RT-PCR analysis of *Fsp1* expression (n = 6). (h) TBARS assay for MDA in the liver extracts from ctrl or *Gpx4* LKO mice fed GAN diet for 40 weeks (n = 6). P = 0.0574. MDA: Malondialdehyde. (i) Immunohistochemical images of 4-HNE detected by DAB staining in the liver of ctrl or *Gpx4* LKO mice fed GAN diet for 40 weeks (n = 6). Quantification was performed on 4-HNE^{+} areas indicated by blue pseudo-coloring. Statical significance was determined by two-tailed Students' t-test. $^{****}P < 0.0001$.

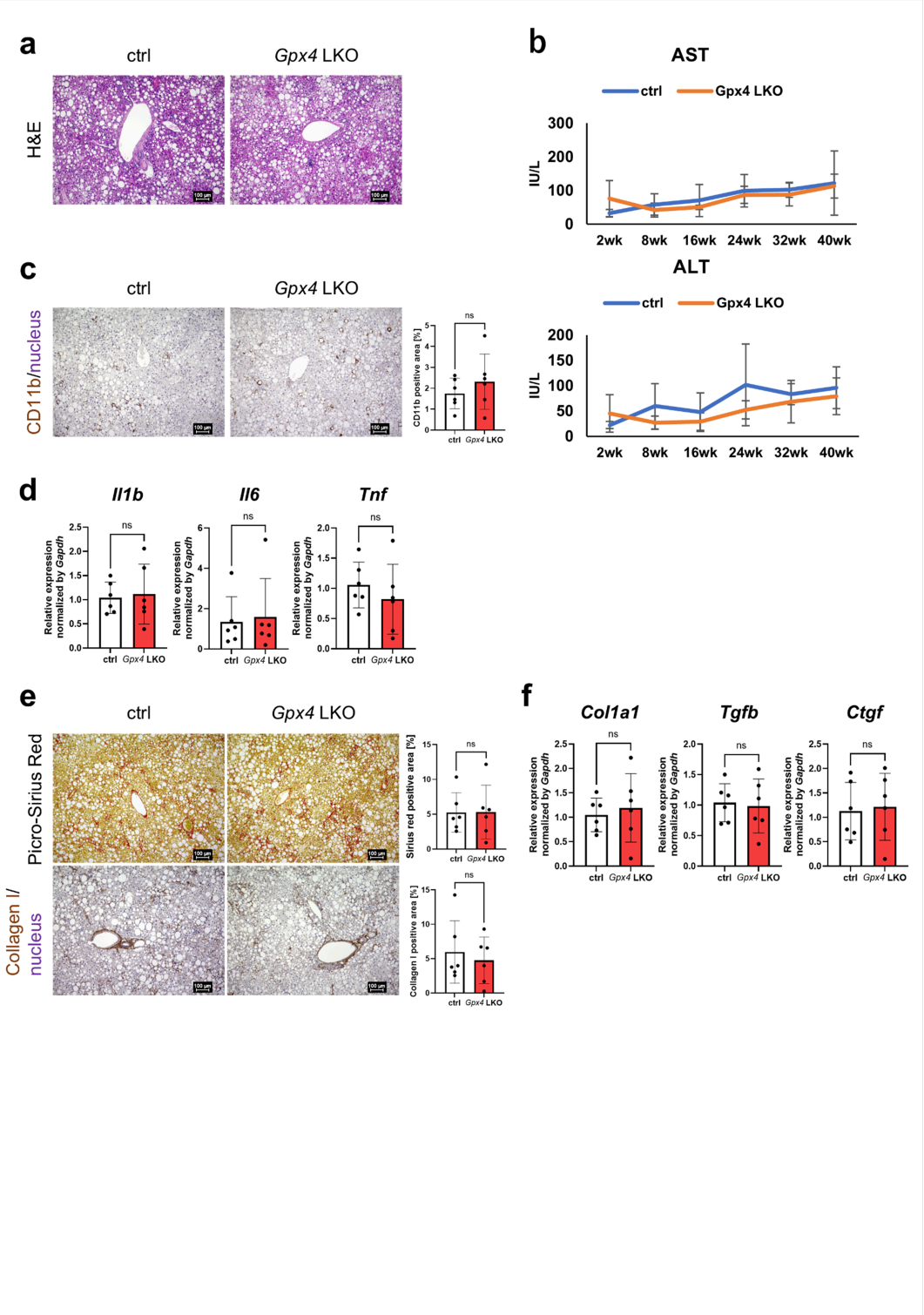


Figure 2

Figure 2

Evaluation of MASH pathology in *Gpx4* LKO mice

(a) H&E staining of liver sections from GAN-diet-fed ctrl or *Gpx4* LKO mice. (b) Measurement of serum liver injury markers, ALT and AST, in ctrl or *Gpx4* LKO mice fed GAN diet for 40 weeks. (c) Immunohistochemical images of CD11b detected by DAB staining in the liver of ctrl or *Gpx4* LKO mice

fed GAN diet for 40 weeks (*n* = 6). (d) Quantitative RT-PCR analysis of inflammatory cytokine expression (*n* = 6). All data are normalized to *Gapdh.* (e) Representative images of Picro-Sirius Red staining (top figure) and immunohistochemistry of Collagen I (bottom figure) in the liver of mice fed GAN diet for 40 weeks (*n* = 6). Quantitative analysis of fibrotic area detected by Picro-Sirius Red staining and immunostaining for Collagen I is shown (*n* = 6). (f) Quantitative RT-PCR analysis of fibrosis-related gene expression (*n* = 6). Statical significance was determined by two-tailed Students' *t*-test. ns: not significant.

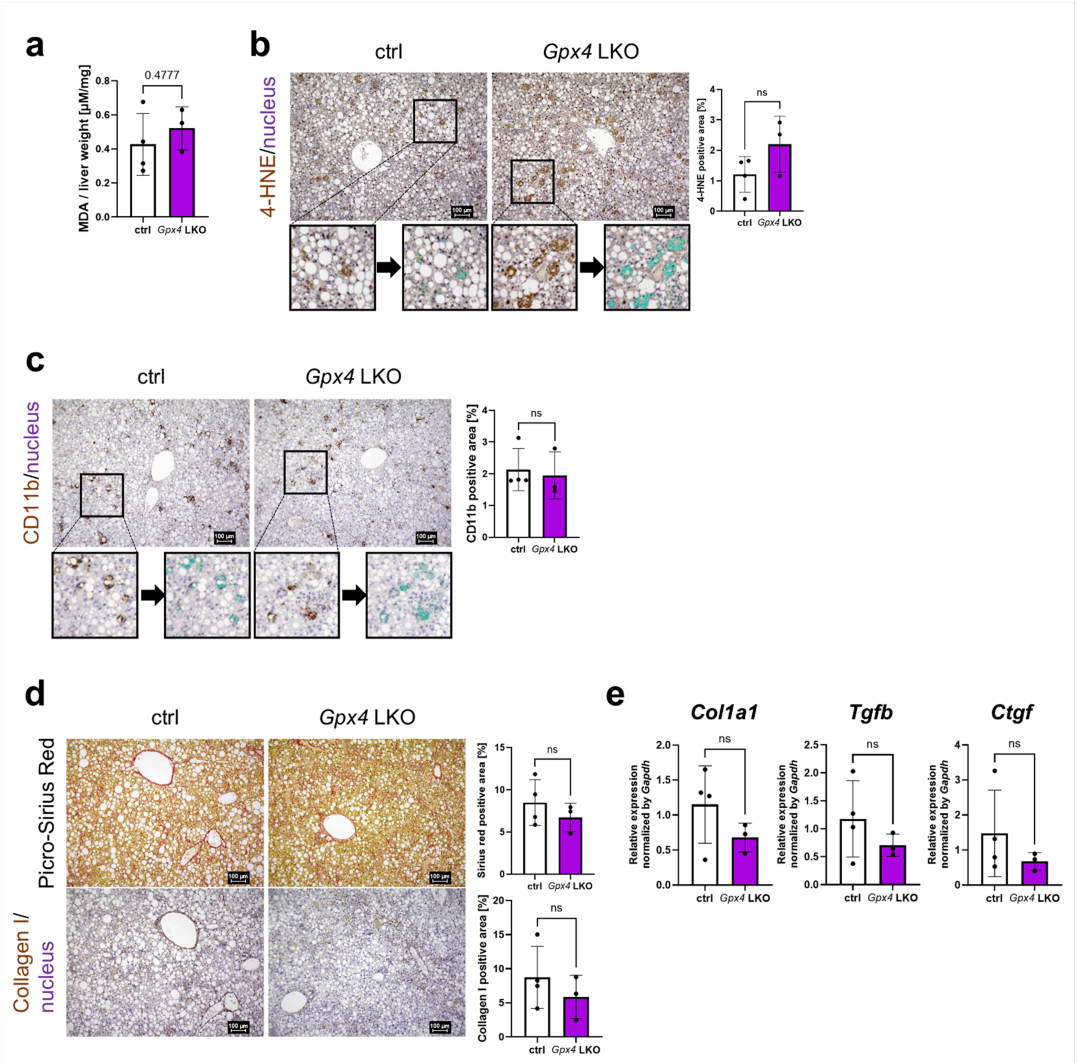


Figure 3

Figure 3

Evaluation of MASH pathology in *Gpx4* LKO mice fed CDAHFD

(a) TBARS assay for MDA in the liver extracts from ctrl or *Gpx4* LKO mice fed CDAHFD for 24 weeks (ctrl: *n* = 4, *Gpx4* LKO: *n* = 3). (b) Immunohistochemical images of 4-HNE detected by DAB staining in the liver of ctrl or *Gpx4* LKO mice fed CDAHFD for 24 weeks (ctrl: *n* = 4, *Gpx4* LKO: *n* = 3). 4-HNE^{+} areas identified by blue pseudo-coloring were used for quantification. (c) Immunohistochemical images of CD11b detected by DAB staining in the liver of ctrl or *Gpx4* LKO mice fed CDAHFD for 24 weeks. (ctrl: *n* = 4, *Gpx4* LKO: *n* = 3). CD11b^{+} areas identified by blue pseudo-coloring were used for quantification. (d) Representative images of liver fibrosis by Picro-Sirius Red staining in the liver of ctrl or *Gpx4* LKO mice fed CDAHFD for 24 weeks. Quantitative analysis of fibrotic areas detected by Picro-Sirius Red staining is shown (ctrl: *n* = 4, *Gpx4* LKO: *n* = 3). DAB-stained images of Collagen I in the liver of ctrl or *Gpx4* LKO mice fed CDAHFD for 24 weeks. (e) Quantitative RT-PCR analysis of fibrosis-related gene expression in the liver of ctrl or *Gpx4* LKO mice fed CDAHFD for 24 weeks (ctrl: *n* = 4, *Gpx4* LKO: *n* = 3). All data are normalized to *Gapdh*. Statical significance was determined by two-tailed Students' *t*-test. ns: not significant.

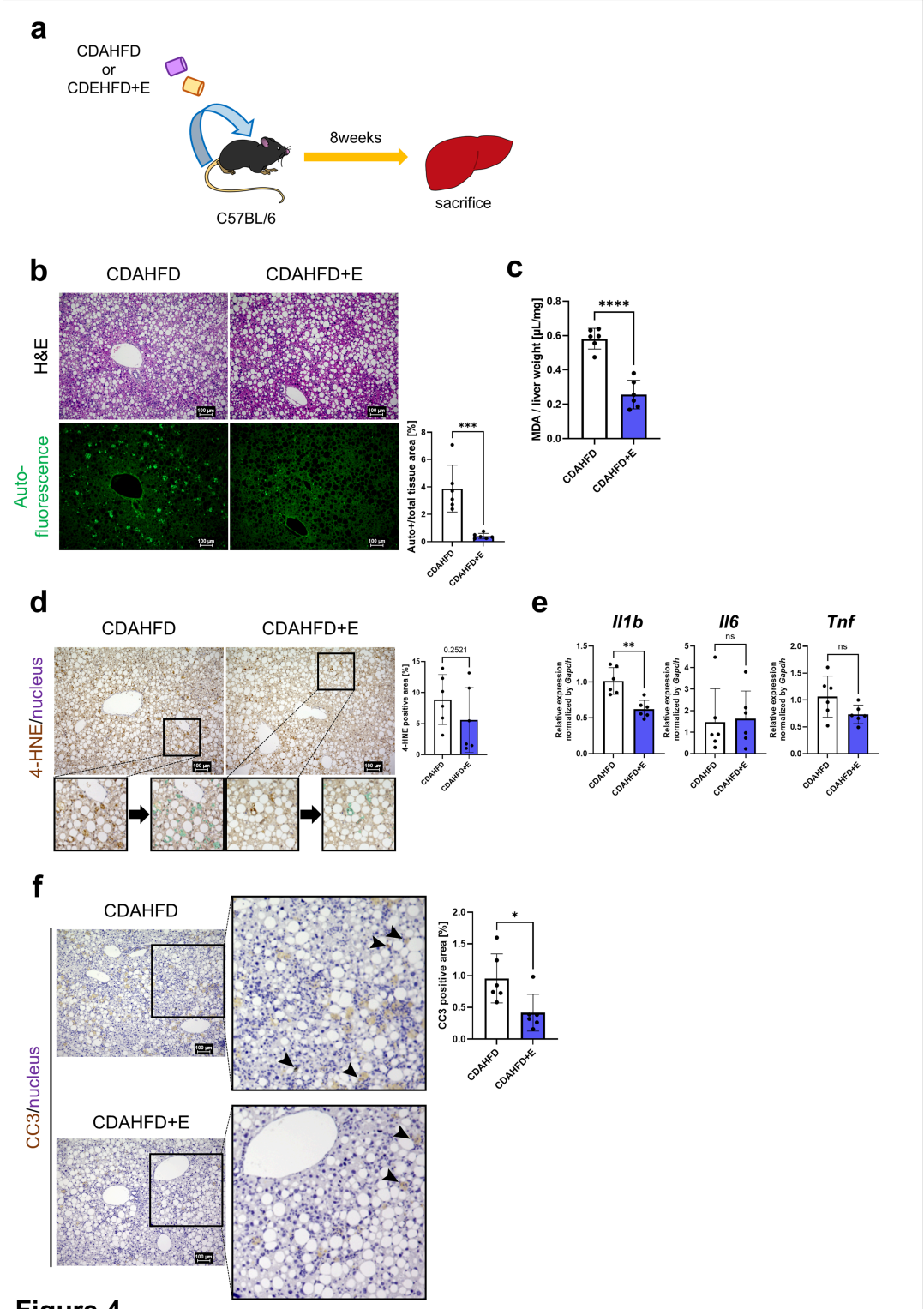


Figure 4

Figure 4

Inhibition of ferroptosis in murine model of MASH by vitamin E administration

(a) Experimental design for murine model of MASH fed CDAHFD or CDAHFD+E for 8 weeks (*n* = 6). (b) Representative images of H&E staining (top figure) and autofluorescence (bottom figure) in the liver of mice fed CDAHFD or CDAHFD+E for 8 weeks. Quantitative analysis of autofluorescence is shown (*n* = 6).

(c) TBARS assay for MDA in the liver extracts from mice fed CDAHFD or CDAHFD+E for 8 weeks (*n* = 6). (d) Immunohistochemical images of 4-HNE detected by DAB staining in the liver of mice fed CDAHFD or CDAHFD+E for 8 weeks. Representative images and quantitative analysis of DAB-stained area per field of view (*n* = 6). ns: not significant. 4-HNE^{+} areas identified by blue pseudo-coloring were used for quantification. (e) Quantitative RT-PCR analysis of inflammatory cytokine expression (*n* = 6). (f) Immunohistochemical images of CC3 detected by DAB staining in the liver of mice fed CDAHFD or CDAHFD+E for 8 weeks. Representative images and quantitative analysis of DAB-stained area per field of view are shown (*n* = 6). (g) Immunohistochemical images of CD11b detected by DAB staining in the liver of mice fed CDAHFD or CDAHFD+E for 8 weeks (*n* = 6). (h) Representative images of fibrosis by detected Picro-Sirius Red staining (top figure) and immunohistochemistry of Collagen I (bottom figure) in the liver of mice fed CDAHFD or CDAHFD+E for 8 weeks. Quantitative analysis of fibrotic area detected by Picro-Sirius Red staining and immunostaining for Collagen I is shown (*n* = 6). (i) Quantitative RT-PCR analysis of inflammatory cytokine expression in mice fed CDAHFD or CDAHFD+E for 8 weeks (*n* = 6). All data are normalized to *Gapdh.* Statical significance was determined by two-tailed Students' *t*-test. $^{*}P < 0.05$; $^{**}P < 0.01$; $^{***}P < 0.001$; $^{***}P < 0.001$; ns, not significant.

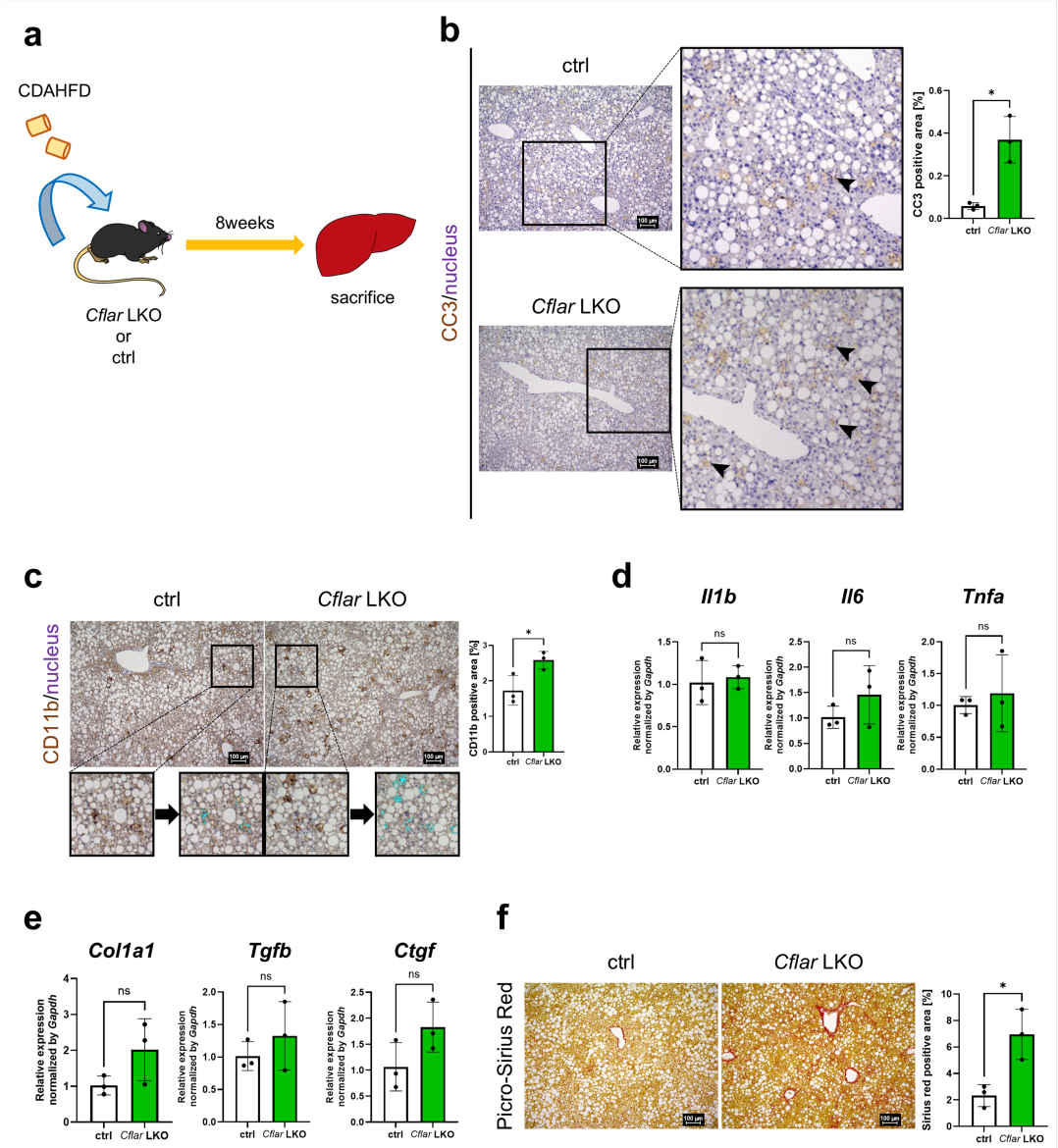


Figure 5

Figure 5

Evaluation of MASH pathology in *Cflar* LKO mice fed CDAHFD

(a) Experimental design for ctrl or *Cflar* LKO mice fed CDAHFD for 8 weeks (n = 3). (b) DAB-stained images of CC3 in the liver of ctrl or *Cflar* LKO mice fed MASH diet (CDAHFD) for 8 weeks (n = 3). Representative images and quantitative analysis of DAB-stained area per field of view are shown. (c)

Immunohistochemical images of CD11b detected by DAB staining in the liver of ctrl or *Cflar* LKO mice fed CDAHFD for 8 weeks (n = 3). (d) Quantitative RT-PCR analysis of inflammatory cytokine expression in the liver of ctrl or *Cflar* LKO mice fed CDAHFD for 8 weeks (n = 3). (e) Quantitative RT-PCR analysis of fibrosis-related gene expression in the livers of ctrl or *Cflar* LKO mice fed CDAHFD for 8 weeks (n = 3). (f) Representative images of liver fibrosis detected by Picro-Sirius Red staining in the liver of ctrl or *Cflar* LKO mice fed CDAHFD for 8 weeks (n = 3). Quantitative analysis of fibrotic area detected by Picro-Sirius Red staining is shown (n = 3). All data are normalized to *Gapdh*. Statical significance was determined by two-tailed Students' *t*-test. $^{*}P < 0.05$; ns, not significant.

Supplementary Files

This is a list of supplementary files associated with this preprint. Click to download.

- OriginalWB1Figure1f.tif
- OriginalWB2SupplementalFigureS1e.tif
- SpplementalFigureS1.tif
- Table.tif
- SupplementalFigureS2.tif